

MOX-Report No. 04/2016

**Finite element simulations of the active stress in the
imaginal disc of the *Drosophila Melanogaster***

Pettinati, V.; Ambrosi, D; Ciarletta P.; Pezzuto S.

MOX, Dipartimento di Matematica
Politecnico di Milano, Via Bonardi 9 - 20133 Milano (Italy)

mox-dmat@polimi.it

<http://mox.polimi.it>

Finite element simulations of the active stress in the imaginal disc of the *Drosophila Melanogaster*

V. Pettinati, D. Ambrosi,

MOX–Dipartimento di Matematica, Politecnico di Milano,
piazza Leonardo da Vinci 32, 20133 Milano, Italy

P. Ciarletta

CNRS and Sorbonne Universitiés, UPMC Univ Paris 06, UMR7190, Institut
Jean le Rond d’Alembert, 4 place Jussieu case 162, 75005 Paris France
MOX-Politecnico di Milano and Fondazione CEN, piazza Leonardo da Vinci 32,
20133 Milano, Italy

S. Pezzuto

Institute of Computational Science, Faculty of Informatics,
via Giuseppe Buffi 13, 6900 Lugano Switzerland

December 17, 2015

Abstract

During the larval stages of development, the imaginal disc of *Drosophila Melanogaster* is composed by a monolayer of epithelial cells, which undergo a strain actively produced by the cells themselves. The well-organized collective contraction produces a stress field that seemingly has a double morphogenetic role: it orchestrates the cellular organization towards the macroscopic shape emergence while simultaneously providing a local information on the organ size. Here we perform numerical simulations of such a mechanical control on morphogenesis at a continuum level, using a three-dimensional finite model that accounts for the active cell contraction. The numerical model is able to reproduce the (few) known qualitative characteristics of the tensional patterns within the imaginal disc of the fruit fly. The computed stress components slightly deviate from planarity, thus confirming the previous theoretical assumptions of a nonlinear elastic analytical model, and enforcing the hypothesis that the mechanical stress may act as a size regulating signal that locally scales with the global dimension of the domain.

1 Introduction

The *Drosophila Melanogaster*, commonly known as "fruit fly", has been extensively studied over the last decades as a system model in developmental biology. During the larval stages of

development, it is composed by a monolayer of few tens of endothelial cells, also known as the *wing imaginal disc*. Morphogenetic events later control cell division, death and rearrangement in a spatially coordinated manner, giving rise to the three-dimensional (3D) adult wing, which is a folded structure with a macroscopic size, eventually made of several thousands of epithelial cells. The control in shape and size in the imaginal disc is still a very debated matter among biologists. In particular, it has not yet been fully understood which communication mechanisms locally convey the global information about the disc size, so that the individual cells can adjust and coordinate their mitotic rate during the larval development.

Morphogens are soluble factors produced by the cells themselves which diffuse and degrade at finite rates and many examples have been identified inside the imaginal disc. Such morphogens have been considered as natural candidates for size control, since an abnormal growth pattern is observed in the wing if their expression is somehow inhibited or unregulated. Notwithstanding, their ability to convey the global information of the size of the wing is controversial: in fact, they are characterized by a short-range action and, most importantly, in the observed reaction-diffusion dynamics neither their concentration nor their concentration gradient invariably *scale* with size.

A possible mechanism of size control that enforces the due *scaling* characteristics has been proposed by Wartlick and coworkers [3], who have intensively focused on the distribution within the wing imaginal disc of a particular morphogen, the Decapentaplegic (Dpp), in the third larval stage. Wartlick's model is based on two experimental evidences:

- The Dpp distribution is described by a reaction-diffusion equation and its spatial dynamics is fast with respect to the growth of the disc: both diffusion and decay of Dpp can be assumed to be always in mutual equilibrium so that the mass convection due to the material displacement caused by the cell duplication process does not affect the morphogen concentration field $c(x, t)$.
- The cell duplication rate is homogeneous in space.

These experimental observations clearly highlight the conundrum to conciliate an inhomogeneous morphogen distribution with a homogeneous growth: if the concentration of morphogen diffuses with a constant diffusivity and decays at a fixed rate, it cannot scale with the organ size. Thus, Wartlick and coworkers conjectured the existence of a non-degrading molecule that gets diluted during the cell proliferation. If the degradation rate of Dpp depends linearly on this molecule, the morphogen concentration might scale as the length of the domain and could possibly trigger a homogeneous growth. Even if other growing control mechanisms have been proposed only relying on the concentration of chemical species (as an example, see [5]), a complete explanation of the size determination of the adult wing uniquely in terms of reactive-diffusive agents still remains elusive.

Another possible control mechanism relies on the experimental evidence that the epithelial cells are in a tensional mechanical state during this larval stage, which is generated not by external loads but by some shape changes of the cells themselves. Hufnagel and coworkers [4] argued that this mechanical stress might compensate the decay of morphogen concentration in the periphery of the disc, so that a combination of morphogen diffusion and mechanical effects might regulate the disc growth.

In a more recent paper, Ambrosi and coworkers [15] proposed a mathematical model proving that the mechanical stress could convey local information on global size during the wing morphogenesis. Since the epithelial cells are known to actively deform [7], the presence of an inhomogeneous active contraction, spatially triggered by the morphogen concentration, was found to give rise to a stress distribution embedding the key information about the size of the domain.

According to such a mechanism, all the cells receive the same instructive signal, and therefore they all display the same behavior and stop their duplication process simultaneously when a certain threshold is reached.

In a mathematically formal way, let us state that a generic (chemical, mechanical) signal f can orchestrate the cellular mitosis over a macroscopic affine transformation if it depends on the principal spatial coordinate in the following form:

$$f(R, t) = f_0(R_0)f_1(R/R_0), \quad (1)$$

where R and t denote the spatial and temporal variables respectively and $R_0 = R_0(t)$ stands for the macroscopic length of the domain. In this scenario, the scalar function f_0 provides the absolute information of the domain size, while the self-similar scalar function f_1 is constant for a given individual cell because of the homogeneous growth process.

Thus, using a nonlinear elastic model and assuming a two-dimensional (2D) plane strain–plane stress assumption, it has been shown that prescribing an active contraction in an inner circular portion of the imaginal disc (possibly dictated by the higher concentration of morphogens), the elastic equilibrium imposes a stress distribution of the form given by (1). Since this active contraction has been experimentally observed in the circumferential direction [8], the hoop stress can be exactly expressed in the form (1), it is compressive and grows in each fixed spatial position as the disc becomes larger. These qualitative results are in agreement with recent experimental observations [6].

In this work we corroborate and extend this mechanical idea to the case of a fully 3D domain by applying a novel numerical simulation tool. We adopt a finite element code to determine the stress pattern induced by an inhomogeneous active contraction in a 3D disc. We consider both an illustrative geometry, made of a thin circular plate, and the real shape of the wing imaginal disc. The numerical simulations allow us to explore contractility patterns with increasing complexity: both radial and biaxial configurations in the morphogens' concentration can be set on the basis of line sources possibly determining the active region. The flexibility of the proposed numerical tool allows us to enforce different symmetries to take into account the experimental reports obtained by different techniques. In particular, we address both the configuration considered by Nienhaus et al. [6] and Mao et al. [8], who suggest a radial symmetry in the active strain, and the bilateral configuration reported by Landsberg et al. [19]. In both cases, we validate numerically in a 3D geometry the simplifying assumptions that are at the basis of the previous 2D analytical results.

The paper is organized as follows. Basic notions of continuum mechanics are resumed in section 2. The well-posedness of the mathematical problem and the numerical method are illustrated in section 4. Sections 3 and 5 are devoted to the analytical determination and numerical approximation of the mechanical signal which conveys the information about the length of the domain in the case of a 2D and 3D domain, respectively. The three-dimensional geometries considered in section 5 are a thin plane and then the real shape of the wing imaginal disc. The numerical results on the strain and stress patterns obtained are finally collected and discussed in section 6, together with some conclusive remarks.

2 Kinematic and constitutive assumptions

Let us consider the imaginal disc as a continuous body \mathcal{B} initially occupying a spatial domain $\Omega_0 \subseteq \mathbb{R}^3$ in the reference configuration. The position vector in the reference configuration is indicated by the material vector \mathbf{X} . Let φ denote the motion function that describes the deformation between Ω_0 and the current configuration Ω , so that the spatial position vector is given by:

$$\mathbf{x} = \varphi(\mathbf{X}, t),$$

therefore the displacement field reads:

$$\mathbf{u}(\mathbf{X}, t) = \mathbf{x} - \mathbf{X} = \boldsymbol{\varphi}(\mathbf{X}, t) - \mathbf{X}.$$

The deformation gradient tensor \mathbf{F} is the material gradient of the motion:

$$\mathbf{F}(\mathbf{X}, t) = \frac{\partial \boldsymbol{\varphi}(\mathbf{X}, t)}{\partial \mathbf{X}} = \text{Grad } \mathbf{x}(\mathbf{X}, t) = \mathbf{I} + \text{Grad } \mathbf{u},$$

where \mathbf{I} is the identity matrix, and

$$J(\mathbf{X}, t) = \det \mathbf{F}(\mathbf{X}, t),$$

is the determinant Jacobian of the transformation, describing the change from the infinitesimal volume $d\mathbf{X}$ in the reference configuration to the infinitesimal volume in the actual configuration $J(\mathbf{X}, t) d\mathbf{x}$.

Since the epithelial cells are mainly composed by water, the incompressibility constraint applies:

$$J = 1 \quad \text{for every } \mathbf{X} \in \Omega_0.$$

In nonlinear elasticity, it is useful to describe the deformation introducing the left Cauchy–Green tensor \mathbf{C} , the right Cauchy–Green tensor \mathbf{B} and the Green strain tensor \mathbf{E} , defined as:

$$\mathbf{C} = \mathbf{F}^T \mathbf{F}, \quad \mathbf{B} = \mathbf{F} \mathbf{F}^T, \quad \mathbf{E} = \frac{1}{2}(\mathbf{C} - \mathbf{I}).$$

The local balance of the linear and angular momentum, in the actual configuration and in absence of external forces and inertia, rewrites:

$$\begin{cases} \text{div } \mathbf{T} = 0, & \text{for } \mathbf{x} \in \Omega, \\ \mathbf{T} = \mathbf{T}^T, \\ \mathbf{T} \mathbf{n} = 0, & \text{on } \Gamma_N, \end{cases} \quad (2)$$

where div is the spatial divergence operator, \mathbf{T} is the Cauchy stress tensor, Γ_N is the traction-free portion of boundary, and \mathbf{n} is its outward normal. Using the Piola's transformation, the equilibrium equations (2) in the material configuration read:

$$\begin{cases} \text{Div } \mathbf{F} \mathbf{S} = 0, & \text{for } \mathbf{X} \in \Omega_0, \\ \mathbf{F} \mathbf{S} \mathbf{N} = 0, & \text{for } \mathbf{X} \in \Gamma_N, \end{cases} \quad (3)$$

where Div is the material divergence operator, \mathbf{N} is the outward normal in the reference configuration, and \mathbf{S} is the second Piola–Kirchhoff tensor, defined as:

$$\mathbf{S} = J \mathbf{F}^{-1} \mathbf{T} \mathbf{F}^{-T}.$$

The disc will be considered as an hyperelastic body, so that the second Piola–Kirchhoff tensor can be described by the means of a scalar strain–energy density function $\mathcal{W}: \Omega_0 \times \text{Lin}^+ \rightarrow \mathbb{R}^+$, such that:

$$\mathbf{S} = 2 \frac{\partial \widehat{\mathcal{W}}}{\partial \mathbf{C}}$$

where $\widehat{\mathcal{W}}(\mathbf{X}, \mathbf{C}) = \widehat{\mathcal{W}}(\mathbf{X}, \mathbf{F}^T \mathbf{F}) = \mathcal{W}(\mathbf{X}, \mathbf{F})$. We remark that for any choice of $\widehat{\mathcal{W}}(\mathbf{X}, \mathbf{C})$, \mathbf{S} is always symmetric, since \mathbf{C} is symmetric.

3 The axial-symmetric 2D approximation: analytical results

The symmetric shape of the wing imaginal disc suggests to sketch it as a circular disc spanned by a polar system of coordinates (R, Θ) . The disc can be therefore modelled as a circle of radius R_0 , so that the displacement field \mathbf{u} has radial component only: $u = u(R)$.

The force per unit surface actively produced by the cells is mathematically encoded in an active strain formulation, formally corresponding to a multiplicative decomposition of the gradient of deformation tensor into two contributions: a passive elastic term \mathbf{F}_e and an active term \mathbf{F}_a , so that

$$\mathbf{F} = \mathbf{F}_e \mathbf{F}_a. \quad (4)$$

The active component \mathbf{F}_a requires further constitutive assumptions, whilst the hyperelastic strain energy uniquely depends on $\mathbf{F}_e = \mathbf{F} \mathbf{F}_a^{-1}$.

We assume that the wing imaginal disc is made of an incompressible isotropic neo-Hookean material, characterized by the following strain-energy function:

$$\widehat{\mathcal{W}}(\mathbf{C}_e) = \frac{\mu}{2} (\text{tr } \mathbf{C}_e - 3) = \frac{\mu}{2} (\mathbf{C} : \mathbf{C}_a^{-1} - 3), \quad (5)$$

where μ is the shear modulus, $\mathbf{C}_e = \mathbf{F}_e^T \mathbf{F}_e$ and $\mathbf{C}_a = \mathbf{F}_a^T \mathbf{F}_a$.

The active strain \mathbf{F}_a can be spatially triggered by the morphogens' concentration, which evolves in time following a reaction-diffusion dynamics and typically generates a *short-range* signal. Let $R_i \ll R_0$ be the distance from the center of the disc where the morphogen concentration is not anymore detectable by the cells, we suppose that tissue actively deforms for $R < R_i$, while it behaves like inert matter elsewhere. According to some recent experimental observations [2, 6], we assume that R_i scales as R_0 , which implies that the ratio $\frac{R_i}{R_0}$ remains a constant during the whole developmental process. It follows that $\mathbf{F}_a = \mathbf{I}$ for $R > R_i$, while it has to be prescribed in a different way according to the observed cell shape distortion in the inner region, which we call the *active region*.

On the basis of the reported observations [8], we assume that \mathbf{F}_a in the active region is given by

$$\mathbf{F}_a = \begin{bmatrix} \delta & 0 \\ 0 & \gamma \end{bmatrix}$$

where δ and γ account for microstructural active strain in the radial and circumferential direction, respectively. Denoting by $u = r(R) - R$ the radial displacement, we impose the incompressibility constraint $\det \mathbf{F}_e = 1$, and the following interface and boundary conditions for the displacement:

$$\begin{aligned} u(0) &= 0, & u(r_i^-) &= u(r_i^+) \\ T_{rr}(r_0) &= 0, & T_{rr}(r_i^-) &= T_{rr}(r_i^+). \end{aligned}$$

Solving the stress balance equations (2), the radial and hoop components of the Cauchy stress can be expressed as a function of the material coordinate R as:

$$T_{rr} = T_{rr}(R_0) + \mu \left(\frac{\delta}{\gamma} - \frac{\gamma}{\delta} \right) \log \left(\frac{R}{R_0} \right), \quad (6)$$

$$T_{\theta\theta} = \mu \left(\frac{\delta}{\gamma} - \frac{\gamma}{\delta} \right) \left(1 + \log \left(\frac{R}{R_i} \right) \right) + T_{rr}(R_0), \quad (7)$$

for $R \in (0, R_0)$ and

$$\mathbb{T}_{rr} = \frac{\mu}{2} \left[\log \left(\frac{(R_0^2 + 2\kappa R_i^2)(R^2 + \kappa R_i^2)}{(R^2 + 2\kappa R_i^2)(R_0^2 + \kappa R_i^2)} \right) + \kappa R_i^2 \frac{R^2 - R_0^2}{(R_0^2 + 2\kappa R_i^2)(R^2 + 2\kappa R_i^2)} \right], \quad (8)$$

$$\begin{aligned} \mathbb{T}_{\theta\theta} = \mu & \left[\frac{R^2 + \kappa R_i^2}{R^2} - \frac{R^2}{R^2 + \kappa R_i^2} + \frac{\kappa}{2} R_i^2 \frac{R^2 - R_0^2}{(R_0^2 + 2\kappa R_i^2)(R^2 + 2\kappa R_i^2)} \right. \\ & \left. + \frac{1}{2} \log \left(1 + \frac{\kappa R_i^2 (R^2 - R_0^2)}{(R^2 + 2\kappa R_i^2)(R_0^2 + \kappa R_i^2)} \right) \right], \end{aligned} \quad (9)$$

for $R \in (R_i, R_0)$, where we have set $\kappa = \gamma\delta - 1$.

Since we assume that $R_i \ll R_0$, the cells in $R > R_i$ are subjected to a hoop stress given by equation (9), that can be rewritten as:

$$\mathbb{T}_{\theta\theta} = R_i^2 f_1 \left(\frac{R}{R_i} \right) + f_2 \left(\frac{R}{R_i} \right). \quad (10)$$

For a constant ratio R_i/R_0 , the hoop stress at each given material point provides an information about R_i . Summarizing, the hoop stress produced by the cell contraction in an active region that scales with the domain size: thus, it is a plausible candidate to orchestrate a homogeneous growth of the disc.

The stress field solution of equations (6)–(9) is represented in figures 1 and 2. These results are in agreement with experimental data [6], showing how high stress values arise in the central region of the disc, which increase for each fixed position for a growing domain.

4 Variational formulation and numerical method

The determination of the 3D stress generated by the active cellular contraction in the real geometry of the imaginal disc can be only tackled using a numerical procedure. In this section we illustrate the basic ingredients of the numerical approximation; while the results of the numerical simulations will be discussed in the following section.

For a hyperelastic material over a domain Ω_0 in the reference configuration, the determination of the elastic solution of the balance equations (3) is equivalent to minimize the strain–energy functional that constitutively defines the material. The well–known results from the calculus of variations state that, given a properly defined Sobolev space V , the problem of finding an admissible displacement \mathbf{u} such that the functional

$$\mathcal{F}(\mathbf{u}) := \int_{\Omega_0} \widehat{\mathcal{W}}(\mathbf{X}, \mathbf{C}_e) \det \mathbf{F}_a \, d\mathbf{X} \quad (11)$$

is stationary can be solved if the functional is quasi–convex [20]. A necessary condition for the quasi–convexity of the functional is the rank–one convexity, which implies the strong ellipticity.

The strain–energy for the imaginal disc is assumed to be given by an incompressible neo–Hookean law, as in equation (5), and the active contraction is transversely isotropic along the principal direction defined by the unit vector \mathbf{f} ,

$$\mathbf{F}_a = \gamma_f \mathbf{f} \otimes \mathbf{f} + \gamma_t (\mathbf{I} - \mathbf{f} \otimes \mathbf{f}),$$

where γ_f and γ_t are the distortion in the principal and transverse direction, respectively. Substituting the latter expression into (5) we obtain:

$$\widehat{\mathcal{W}}(\mathbf{C}_e) = \frac{\mu}{2} (\text{tr } \mathbf{C}_e - 3) = \frac{\mu}{2} \left[\frac{1}{\gamma_f^2 \gamma_t^2} (\gamma_f^2 \text{tr } \mathbf{C} + (\gamma_t^2 - \gamma_f^2) \mathbf{C} \mathbf{f} \cdot \mathbf{f}) - 3 \right].$$

Rank-one convexity [10] and polyconvexity [14] can be easily shown for this type of strain-energy, as long as $\gamma_t \geq \gamma_f > 0$.

The incompressibility is handled by means of a Lagrangian multiplier $p \in Q \subset L^2(\Omega_0)$ which enforces the constraint $\det \mathbf{F}_e = 1$. It is however numerically convenient to rewrite the strain-energy in terms of the tensor

$$\bar{\mathbf{F}}_e = (\det \mathbf{F}_e)^{-1/3} \mathbf{F}_e, \quad \bar{\mathbf{C}}_e = (\det \mathbf{C}_e)^{-1/3} \mathbf{C}_e,$$

so that the function the strain energy function is well defined also for compressible materials. Although this redefinition has no substantial effect at a continuum level, it is crucial for the numerical discretization, where in general is not possible to enforce the constraint pointwise, thus ensuring that the strain-energy is correctly evaluated everywhere [11]. The modified functional reads:

$$\mathcal{F}_{\text{inc}}(\mathbf{u}, p) := \int_{\Omega_0} \bar{\mathcal{W}}_e(\mathbf{X}, \bar{\mathbf{C}}_e) \det \mathbf{F}_a \, d\mathbf{X} - \int_{\Omega_0} p (J - \det \mathbf{F}_a) \, d\mathbf{X}. \quad (12)$$

The characterization of the stationary point $(\mathbf{u}, p) \in V \times Q$ of (12) is obtained from the first variation of the functional (12), which reads:

$$\int_{\Omega_0} \mathbf{S} : \text{sym}(\mathbf{F}^\top \text{Grad } \boldsymbol{\eta}) \, d\mathbf{X} - \int_{\Omega_0} q (J - J_a) \, d\mathbf{X} = 0, \quad \text{for every } (\boldsymbol{\eta}, q) \in V \times Q, \quad (13)$$

where $J_a = \det \mathbf{F}_a$, $\text{sym} \circ$ is the symmetric part of the argument and \mathbf{S} is the second Piola-Kirchhoff tensor. For the case of the imaginal disc, the Cauchy stress tensor is given by:

$$\boldsymbol{\tau} = \frac{J_a^{5/3}}{J} \frac{\mu}{\gamma_f^2 \gamma_t^2} \text{dev} \left[\gamma_f^2 \bar{\mathbf{B}} + (\gamma_t^2 - \gamma_f^2) \bar{\mathbf{B}} \mathbf{f} \otimes \mathbf{f} \right] - p \mathbf{1}, \quad (14)$$

where $\text{dev}(\cdot)$ is the deviatoric operator, returning the trace-free part of its argument.

The numerical discretization of the variational problem (13) proceeds as prescribed by the finite element method, by selecting finite dimensional subspaces V_h and Q_h of V and Q , respectively. The nonlinear problem is then solved by means of the Newton's method, which requires the linearized variational problem. We implemented the numerical code in the FENICS framework [16], with quadratic finite elements for the displacement and linear finite elements for the pressure on a tetrahedral (or triangular) mesh.

We conclude this section by mentioning that our implementation can take advantage of possible symmetries of the problem. For instance, in the case of the thin disk, described in the next section, we restrict the problem to the set of axisymmetric solutions of the form:

$$\begin{cases} r = R + u_R(R, Z), \\ z = Z + u_Z(R, Z), \\ \theta = \Theta, \end{cases}$$

where $(r, z, \theta) \in \Omega$ and $(R, Z, \Theta) \in \Omega_0$. In this case, the physical components of the deformation gradient tensor are:

$$\mathbf{F} = \begin{bmatrix} 1 + \frac{\partial u_R}{\partial R} & \frac{\partial u_R}{\partial Z} & 0 \\ \frac{\partial u_Z}{\partial R} & 1 + \frac{\partial u_Z}{\partial Z} & 0 \\ 0 & 0 & \frac{r}{R} \end{bmatrix},$$

while the variational formulation is modified by substituting $d\mathbf{X}$ with $2\pi R d\mathbf{X}$ and integrating only over one section (R, Z) in Ω_0 .

5 The 3D imaginal disc: geometry and experimental facts

The 2D stress fields analytically determined in section 3 qualitatively reproduce some key experimental observations, thus providing a possible communication mechanism for size orchestration. Nevertheless, the two dimensional approximation is to be validated by a quantitative comparison with the results of the 3D numerical simulations. Here we consider different shapes of the active region, with different active contraction in 3D domains: namely a thin cylinder and the real wing imaginal disc shape.

Even if we are aware of the very complex signaling pathways that occur in the imaginal disc during its development, here we do not address in details such a signaling dynamics. In our work we are interested in the presence of soluble factors only in view of their mechanical role; we therefore restrict the discussion on morphogenetic gradients at the minimum degree of detail as necessary for our purpose. In the next paragraph, we start our analysis by summarizing the main known features of the morphogens' diffusive dynamics, with a particular focus on the shape and position of the source lines of the soluble factors which generate the symmetries that we exploit in our modeling approach.

5.1 Sources and patterns of morphogens in the wing imaginal disc

Three different regions can be identified within the wing imaginal disc: the *notum* (proximal), the *hinge* (central) and the *pouch* (distal) (see figure 4). The notum will give rise to the torax of the fruit fly, the pouch to the wing and the hinge to the flexible region between the two.

Among many others, two morphogens play a major role in the developmental biology literature: the Decapentaplegic (Dpp) and the Wingless (Wg). The Dpp source is located along the *anterior–posterior* boundary, the longitudinal axis that divides the disc into two almost equal parts, spreading within the monolayer from a thin central stripe. The production rate, the effective diffusion coefficient and the degradation rate of Dpp have been measured experimentally [1]. The spatial dynamics of Dpp is fast with respect to the growth of the disc: diffusion and decay of Dpp can be assumed to be always in mutual equilibrium so that the mass convection due to the material displacement caused by the cell duplication process does not distort the morphogen concentration field $c(x, t)$. According to recent studies, the Dpp profile scales in space with the disc length and the morphogen concentration adapts to disc size [3, 2]. Notwithstanding, such an experimental observation is criticized by other groups [4]. The biophysical properties of Wg are less known. Like the Dpp, it is a molecule that diffuses away from a localized source to directly instruct cell identity in a concentration–dependent manner, but its distribution in the wing imaginal disc is not as regular as the one for Dpp. It is expressed in two ring–like domains in the hinge region, along the *dorsal–ventral* line, which is orthogonal to the anterior–posterior one and passes through the center of the pouch, and in a broad band in the dorsal part of the disc.

According to several authors [12, 4, 18], the composition in the concentration of Dpp and Wg in the wing pouch can be identified as the instructive signal that regulates the disc growth, produced at the intersection of the two line sources.

5.2 Inhomogeneous active strain in a circular disc

We first consider a simplified model of the imaginal wing disc as a thin circular disc composed by a soft elastic material. The domain Ω_0 is therefore initially characterized by radius R_0 and thickness h , respectively, where from experiments that $h/R_0 \approx 0.04$. A cylindrical material coordinate system (R, Z, Θ) is consistently used. In the following, two different symmetries for the morphogenetic control will be discussed.

5.2.1 Central point source of morphogenetic control

An active region with cylindrical symmetry is generated by a central point source, possibly located at the intersection between the line sources of Dpp and Wg, as depicted in figure 4. The assumption of a radial symmetry is also corroborated by the distribution of the cells in the wing imaginal disc [9] and by the presence of Dachs. In fact, according to [8], the localization of the atypical myosin Dachs correlates with the orientation of cell division and tissue growth in the developing fly wing. Being localized at the distal side of each cell's apical surface, the cells consequently tend to grow preferentially along the P–D axis, forming elongated shapes before dividing (see figure 3).

In the wing of the adult *Drosophila*, the P–D axis is perpendicular to the anterior–posterior axis, but during the larval stages it can be approximated as a line that goes from the center to the periphery of the wing imaginal disc, as established by the combined action of signals emanating from the anterior–posterior and the dorsal–ventral compartments [17]. In our frame of reference, the P–D line is described by the radial axis, therefore the elongation along P–D, in the presence of an incompressible material, is compatible with a circumferential contraction. Therefore, we impose that cells actively contract in the circumferential direction within the region $R < R_i < R_0$, where we employ a multiplicative decomposition of the deformation gradient tensor \mathbf{F} , whose active part in cylindrical coordinates rewrites

$$\mathbf{F}_a = \mathbf{I} + (\gamma - 1) \mathbf{e}_\Theta \otimes \mathbf{e}_\Theta, \quad (15)$$

with $\gamma \in (0, 1]$ and \mathbf{e}_Θ is the spatial unit vector in the circumferential direction. For this case, owning that $J = \det \mathbf{F}_a = \gamma$, the Cauchy stress tensor (14) reads:

$$\mathbf{T} = \mu \operatorname{dev}(\mathbf{B}) + \mu \frac{1 - \gamma^2}{\gamma^2} \operatorname{dev}(\mathbf{B}) \mathbf{e}_\Theta \otimes \mathbf{e}_\Theta - p \mathbf{I}.$$

For $R > R_i$ the material only produces a passive elastic response, i.e. $\gamma = 1$, while for $R < R_i$ the material is subjected to an active contraction with $\gamma < 1$. In $R = R_i$ a discontinuity in the material parameters is present. To overcome numerical issues around this sharp interface, we adopt a smoothed γ of the form:

$$\gamma(R) = \frac{1 - \gamma}{2} \left[1 + \tanh \left(\frac{R - R_i}{\varepsilon} \right) \right] + \gamma$$

and we refine the mesh around $R = R_i$ in order to correctly solve the boundary layer.

The deformation and stress fields resulting from numerical simulation, performed with $\gamma = 0.85$, $R_i = 150 \mu\text{m}$, $R_0 = 3R_i$, and $h = 30 \mu\text{m}$, are shown in figure 5 and 6, respectively. We remark that even if the assumption $R_i \ll R_0$ still remains valid, in the following figures we have reduced the difference between R_i and R_0 with respect to the real one in order to provide a better graphical representation of the results.

The radial and hoop stress components in numerical simulations are depicted in figure 7, and they strongly resemble the corresponding ones in the 2D case. In fact, they are both compressive in the active region, where their magnitude is higher than in the rest of the domain, the axial stress is much smaller than the other components, and none of them changes significantly along z . These numerical results corroborate the assumptions at the basis of our 2D previous planar model.

In every fixed point of the material framework, compression (tension) grows as far as the domain grows. This is in agreement with the calculations carried out with the planar model and, most important, with the experimental observations [6] (see figure 7).

5.2.2 Line source of morphogenetic control

Even if we are not able to identify the specific morphogens triggering the active contraction, we know something about their patterns, since some of them are produced along lines that have been identified in the wing imaginal disc. These source lines can break the axial symmetry of the problem, so that the concentration field becomes genuinely 3D. This scenario, which is hard if not impossible to tackle by analytical tools, can be investigated using the results of the numerical simulations. We therefore further assume that the activating morphogen (possibly Dpp) regulates the tissue growth and concentrates in a thin stripe centered in the anterior–posterior axis, which corresponds to the active region. This setting is supported by the experimental results of Landsberg and coworkers [19]. Starting from the observation that cells which belong to the anterior (posterior) compartment do not mix with the ones of the posterior (anterior) compartment, they argue that the tension along the anterior–posterior boundary is higher than in the other regions of the disc. Using a laser to cut the disc along different lines and observing the tissue displacement, they estimated that the mechanical tension along the anterior–posterior boundary is approximately 2-5 times bigger than in the rest of the tissue. Using a Cartesian frame of reference (x, y, z) with origin in the center of the disc, such that the disc is symmetric about the plane $z = 0$, and representing the anterior–posterior axis by the y -axis, the active region is defined by $|x| < L_c$, with $L_c \ll R_0$. Within this region we impose an active contraction along the y -axis. In this case, the tensor that describes the active contraction is expressed in a Cartesian basis and reads

$$\mathbf{F}_a = \mathbf{I} + (\gamma - 1) \mathbf{e}_2 \otimes \mathbf{e}_2.$$

The computed stress distribution for $\gamma = 0.85$ is shown in figure 8. This result partially contrasts with photoelasticity measurements where the stress distribution in the disc does not exhibit such a bilateral symmetry. While further experimental data are needed to characterize the stress pattern, we remark that the flexibility of the numerical method is in the ability to incorporate different active region: a central stripe of the disc or with a radially symmetric area in the wing pouch.

5.3 Real geometry of the wing imaginal disc

Finally, we consider the real 3D geometry of the wing imaginal disc, with a cylindrical active region centered in the pouch bounded by the material coordinate $R < R_i$. The wing imaginal disc is a thin 3-D structure, whose thickness h is much smaller than the length of the anterior–posterior and dorsal–ventral axes. The origin of the cylindrical system of coordinates is located at the intersection between the anterior–posterior and the dorsal–ventral axes, so that the domain is symmetric above the plane $z = 0$. In the region delimited by a radius $R_i \ll R_0$ we impose an active contraction as defined in equation (15), while $\mathbf{F}_a = \mathbf{I}$ for $R > R_i$. As previously assumed, the material is neo-Hookean and incompressible. We impose in numerical simulations that the material point in the origin has zero displacement, also fixing null rotation and no load applied at the boundary. We have run our finite element solver to find the solution of the stress balance equation. The results are reported in figures 8 and 9.

As expected, the magnitude of the stress is considerably higher in the center than in the periphery of the disc and for small values of R the disc is under compression both in radial and hoop components; moreover the magnitude of the z -component of the stress is negligible with respect to the others. We can conclude that the results we had obtained with a 2-D domain are able to qualitatively capture the essential stress behavior of a realistic 3D geometry. The results of our numerical simulations are reported in figures 9, and can be compared with the existing stress measures reported from photoelasticity experiments, which are reproduced in figure 10. We

can notice that the pattern of the stress obtained experimentally can be qualitatively reproduced by our numerical simulations.

6 Final remarks

The 3D stress field produced by the cells contractility in a wing imaginal disc of the fruit fly has been computed using a finite element code under the assumption that the cell monolayer behaves elastically on the time scale of interest.

The first result of this work is a validation of analytical results previously obtained on the basis of an assumption of plane strain. Our simulations confirm that the planar components of the stress in the fully 3D setting strongly resemble the ones obtained in the 2D case, thus confirming that the planar axialsymmetric approximation is able to catch the relevant features of the stress distribution. Moreover, the z -components of the computed stress is much smaller than the other components and do not significantly vary along the thickness, thus supporting the simplifying 2D assumptions. The quasi planarity of the solution therefore confirms that the stress or its gradient can be a mechanical signal that provides information to the cells about the growth of the wing imaginal disc, thus providing a suitable control mechanism on its final size. This signal is compatible with the experimentally observed homogeneous growth, since it changes in time for each individual cell as a function of the domain length: when the proper domain size is reached, all the cell receive the same signal and they simultaneously slow down their duplication, eventually stopping.

In our 3D numerical simulations the wing imaginal disc is first modeled by a thin cylinder and then represented by its real shape. In both cases the axial stress is negligible compared to the other components and this result validates the analytical solutions obtained in the plane.

The second result of this work is that the numerical simulations reproduce a stress pattern in qualitative agreement with recent experimental observations. The adopted radial symmetry seems to be the most suitable choice at the light of some experimental results [6, 8], supporting the strategy to approximate analytically the imaginal disks as circles of radii R_0 and $R_i < R_0$, respectively. Moreover, the flexibility of the numerical framework allows us to manage different shapes of the active region. In contrast with works that report a stress magnitude that decreases as the distance from the center of the domain increases [6], some studies suggest a bilateral stress distribution because they reproduce a tension that is maximum along the anterior–posterior boundary [19].

The mathematical model contains a very limited number of material and biological parameters (the shear modulus, the micro-strain ratio, the radius of the active region). More experimental data are definitely needed to determine the values of the stress components in the wing imaginal disc, however our model seems encouraging for its flexibility in incorporating further mechanobiological information as soon as available.

References

- [1] Kicheva A, Pantazis P, Bollenbach T, Kalaidzidis Y, Bittig T, Jülicher F and Gonzalez–Gaitan M (2007) Kinetics of morphogen gradient formation. *Science*, 315: 521–525
- [2] Wartlick O, Mumcu P, Kicheva A, Bittig T, Seum C, Jülicher F and Gonzalez–Gaitan M (2011) Dynamics of Dpp signaling and proliferation control, *Science*, 331: 1154–1159

- [3] Wartlick O, Mumcu P, Jülicher F and Gonzalez-Gaitan M (2011) Understanding morphogenetic growth control – lessons from flies, *Nature Reviews Molecular Cell Biology*, 12:594–604
- [4] Hufnagel L, Teleman AA, Rouault H, Cohen SM and Shraiman BI (2007) On the mechanism of wing size determination in fly development, *Proc. Natl Acad. Sci. USA*, 104:3835–3840
- [5] Ben-Zvi D and Barkai N (2010) Scaling of morphogen gradients by an expansion-repression integral feedback control *Proc. Natl Acad. Sci. USA*, 107: 6924–6929
- [6] Nienhaus U, Aegerter-Wilmsen T and Aegerter CM (2009), Determination of mechanical stress distribution in *Drosophila* wing disc using photoelasticity, *Mechanics of Development*, 126:942-949
- [7] Lo CM, Wang HB, Dembo M and Wang YL (2000) Cell movement is guided by the rigidity of the substrate, *Biophys. J.*, 79(1):144–152
- [8] Mao Y, Tournier AL, Bates PA, Gale JE, Tapon N and Thompson BJ (2011) Planar polarization of the atypical myosin Dachs orients cell division in *Drosophila*, *Genes and Development*, 25:131–136.
- [9] Breen D, Widmann T, Bai L, Jülicher F, Dahmann C, Epithelial Cell Reconstruction and Visualization of the Developing *Drosophila* Wing Imaginal Disc, *IEEE Symposium on Biological Data Visualization (BioVis)*, 2012
- [10] Ambrosi D and Pezzuto S (2012) Active stress vs. active strain in mechanobiology: constitutive issues, *J. Elasticity*, 107(2):199-212.
- [11] Bonet J and Wood RD (1997) *Nonlinear continuum mechanics for finite element analysis*.
- [12] Aegerter-Wilmsen T, Aegerter CM, Hafen E and Basler K, Model for the regulation of size in the wing imaginal disc of *Drosophila*, *Mech. Dev.* 124: 318-326 (2007).
- [13] Pezzuto S, Ambrosi D and Quarteroni A, An orthotropic active-strain model for the myocardium mechanics and its numerical approximation, *European Journal of Mechanics, A/Solids* (2014).
- [14] Jörg S and Neff P (2003) Invariant formulation of hyperelastic transverse isotropy based on polyconvex free energy functions, *Int. J. Sol. Struct.* 40.2:401-445.
- [15] Ambrosi D, Pettinati V and Ciarletta P (2015) Active stress as a local regulator of global size in morphogenesis. *International Journal of Nonlinear Mechanics* (in press).
- [16] Logg A, Wells GW and Hake J (2012) *DOLFIN: A C++/Python finite element library*. Springer Berlin Heidelberg.
- [17] Rogulja D, Rauskolb C and Irvine KD, Morphogen Control of Wing Growth through the Fat Signaling Pathway, *Developmental Cell*, 15: 309–321 (2008).
- [18] Shraiman BI, Mechanical feedback as a possible regulator of tissue growth, *Proc. Natl Acad. Sci. USA* 102: 3318-3323 (2005).
- [19] Landsberg KP, Farhadifar R, Ranft J, Umetsu D, Widmann TJ, Bittig T, Said A, Jülicher F and Dahmann C, Increased cell bond tension governs cell sorting at the *Drosophila* anteroposterior compartment boundary, *Current Biology* 19:1950–1955 (2009).
- [20] Dacorogna B, *Direct Methods in the Calculus of Variation*, Springer (2008).

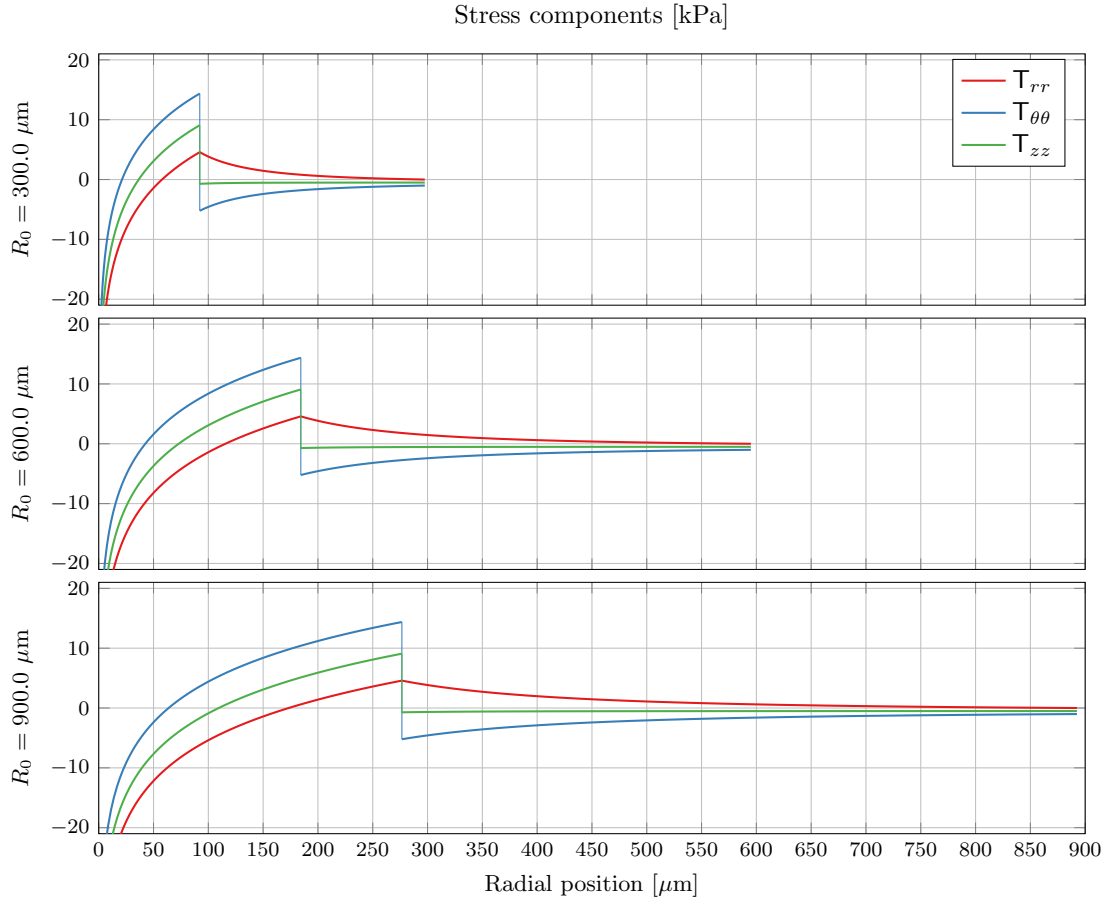


Figure 1: Plot of the radial, circumferential and axial Cauchy stress components (in kPa) versus the actual radial coordinate r at different domain size obtained using a neoHookean strain energy. Material parameters are $\mu = 30$ kPa, $\delta = 1$ and $\gamma = 0.85$. As expected, the radial stress is continuous, while the hoop stress jumps across the interface r_i and changes sign (from compressive to tensional.)

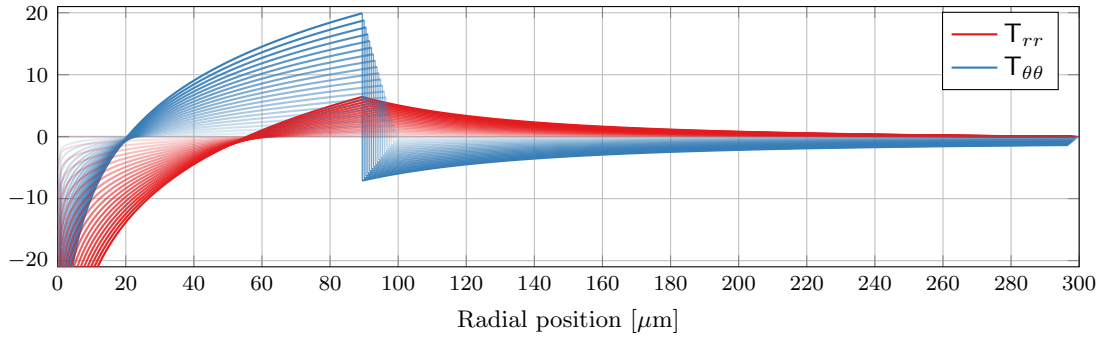


Figure 2: Plot of the radial and circumferential Cauchy stress components (in kPa) versus the actual radial coordinate r at different values of the parameter γ , corresponding to different intensity of the cell contraction. Material parameters are $\mu = 30$ kPa and $\delta = 1$. The lower the value of γ , the higher the opaqueness of the curve. Notice that the interface is located at fixed $R_i = 100$, but the spatial coordinate $r_i(R_i)$ moves to the left for growing contractility

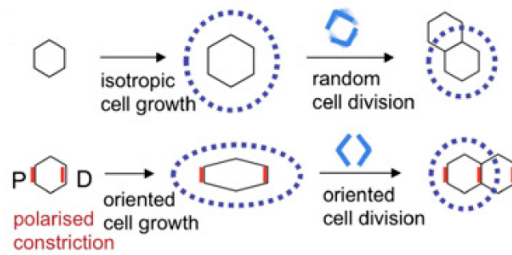


Figure 3: Cell growth, shape, and division in an isotropic (top) and polarized (P–D axis) fashion, generated by Dachs gradient (bottom). Figure adapted with permission from [8].

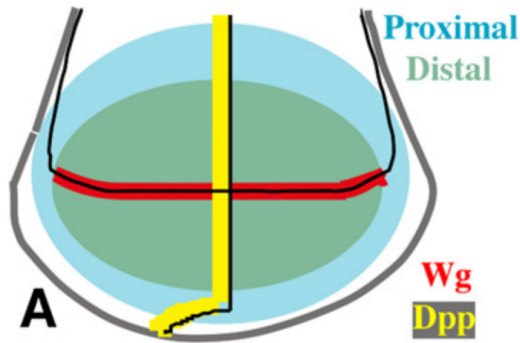


Figure 4: Schematic of a portion of the wing imaginal disc. The proximal and the distal regions are specified by the blue and grey colors, respectively. The Dpp source along the anterior–posterior boundary is marked by the yellow line, while the Wg source along the dorsal–ventral boundary by the red line. Figure adapted with permission from [17].

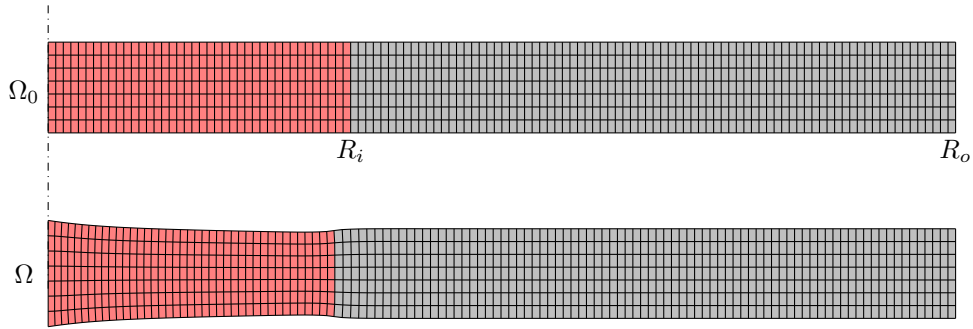


Figure 5: Reference and deformed configuration of a section of the imaginal disc. The red shaded area is the active zone, while the grey area is the purely passive one. The total length is roughly the same, and the displacement in the Z direction is small with respect to the radial deformation. Geometrical and material parameters are $R_i = 150 \mu\text{m}$, $R_o = 3R_i$, $h = 30 \mu\text{m}$, $\mu = 30 \text{ kPa}$ and $\gamma = 0.85$.

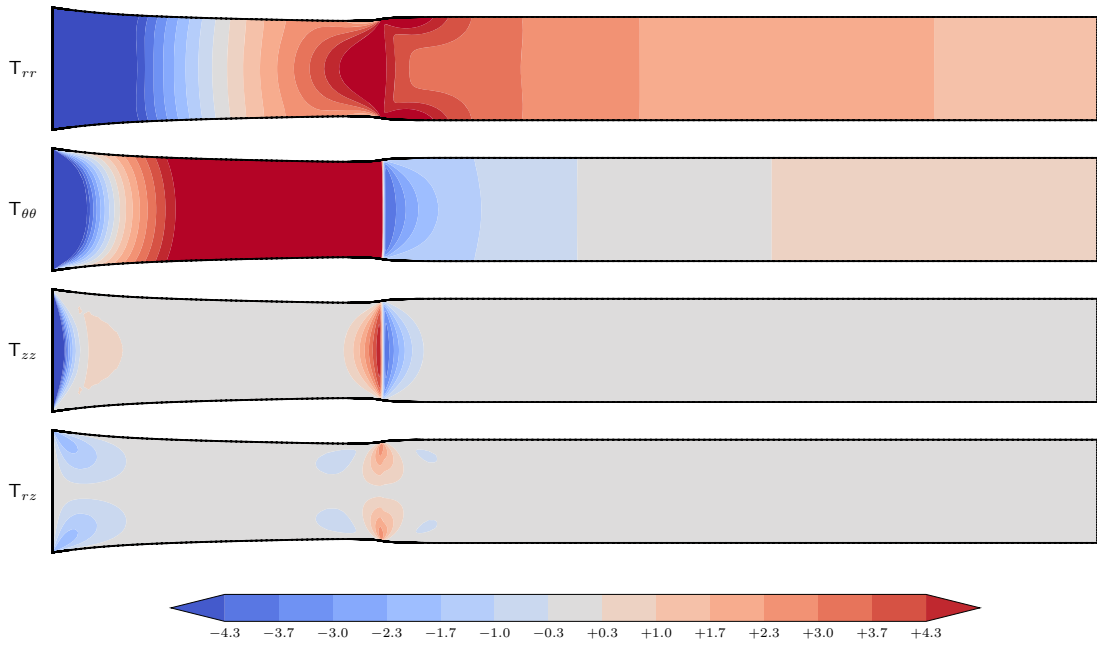


Figure 6: Contour plot of the stress components (in kPa) in a radial section of the imaginal disc. In the active region, the stress magnitude is higher than in the passive zone, where it rapidly approaches zero while getting closer to the outer boundary. Geometrical and material parameters are $R_i = 150 \mu\text{m}$, $R_o = 3R_i$, $h = 30 \mu\text{m}$, $\mu = 30 \text{ kPa}$ and $\gamma = 0.85$.

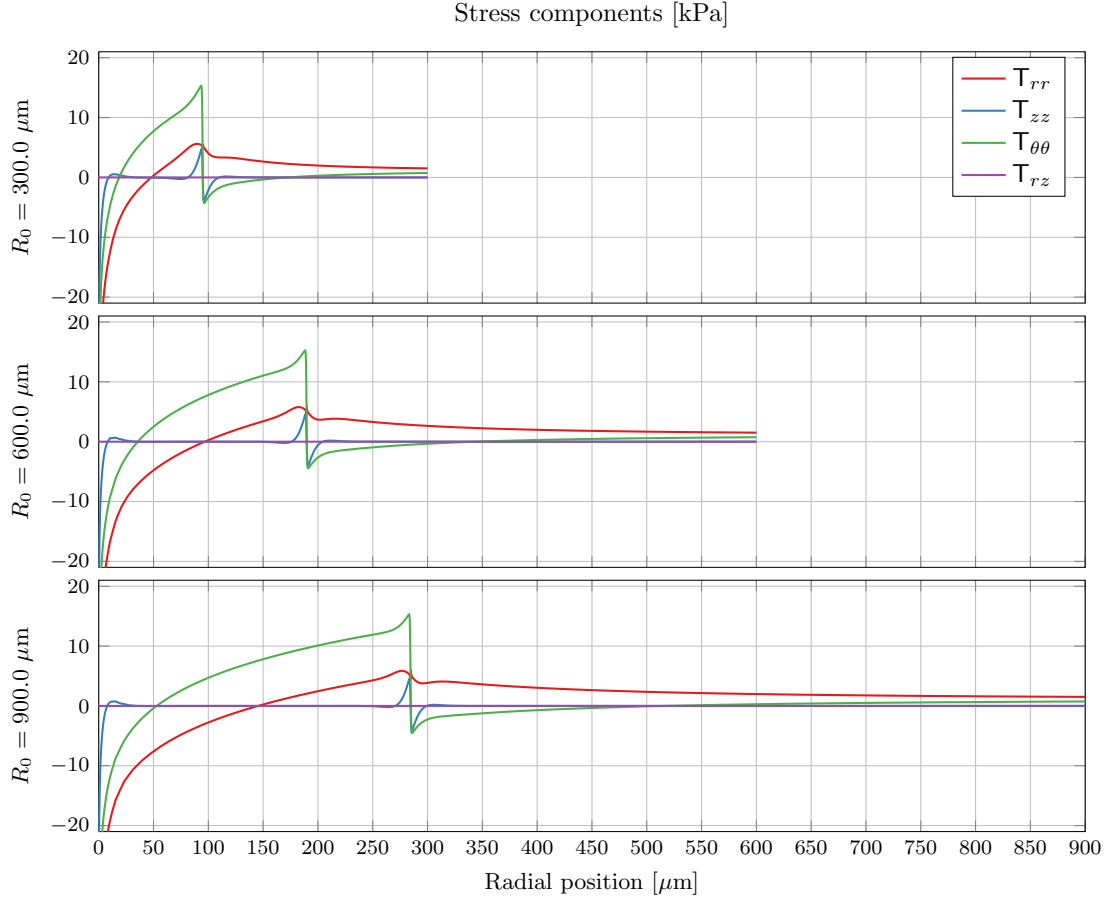


Figure 7: Plot of the Cauchy stress tensor components T_{rr} , T_{rz} , $T_{\theta\theta}$ and T_{zz} along the radial coordinate at $\theta = 0$ and $z = 0$. All these components are negative at the origin, where they are unbounded at the origin. $T_{\theta\theta}$ moves from compressive to tensile within the active region and it reaches the maximum at $R = R_i$, where it is discontinuous and drops to a negative value. In the passive region, its magnitude is considerably lower than in the active one. T_{rr} is a negative increasing function of the radius and its first derivative with respect to r approaches zero after $R = R_i$. The magnitude of T_{zz} is everywhere much smaller than the magnitudes of $T_{\theta\theta}$ and T_{rr} . Geometrical and material parameters are the same as in Figure 6.

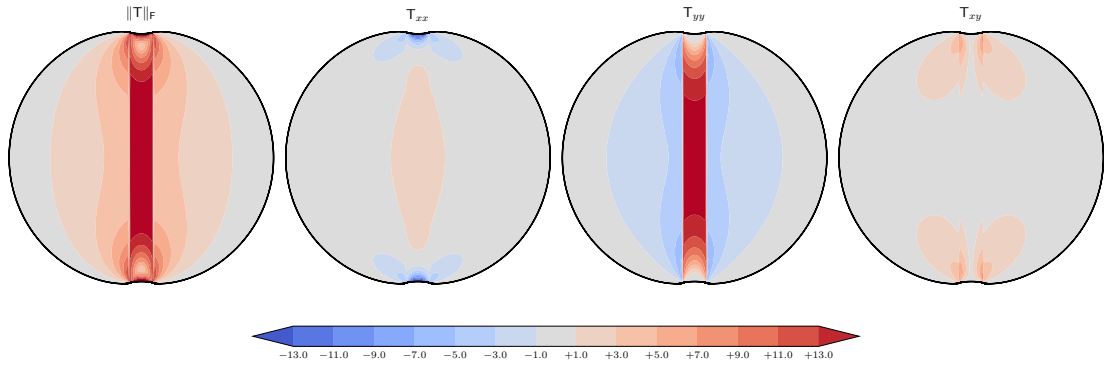


Figure 8: Color plot of the stress distribution (in kPa) computed with active contraction triggered by a Dpp concentration threshold. The active region corresponds to a stripe centered in the anterior–posterior axes and whose thickness is taken to be one tenth of the disc diameter. A bilateral symmetry is found in the stress distribution. The disc diameter is $300 \mu\text{m}$ and its thickness is $h = 15 \mu\text{m}$. Material parameters are $\mu = 30 \text{ kPa}$ and $\gamma = 0.85$.

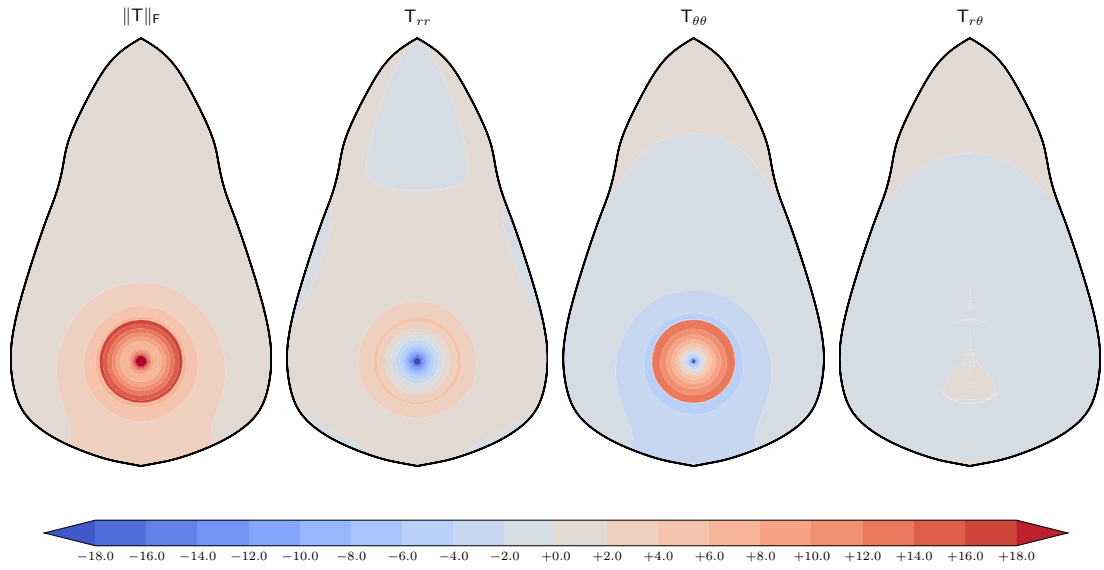


Figure 9: Colour plot of the stress distribution (in kPa) for a slice at $z = 0$ of a wing-shaped domain. The active contraction occurs in a region with a diameter of $300 \mu\text{m}$. In the active region, the stress magnitude is higher than in the passive one, where it approaches zero. Material parameters are $\mu = 30 \text{ kPa}$ and $\gamma = 0.85$.

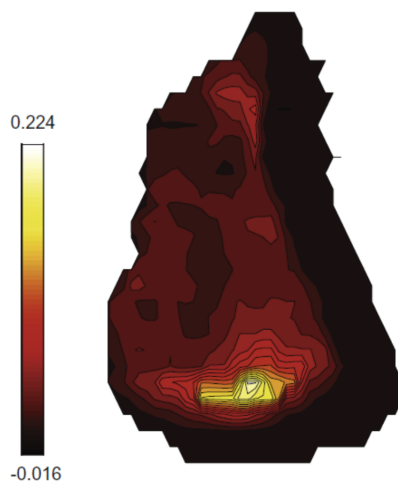


Figure 10: Distribution of retardance in a normal, late stage third instar wing disc. The retardance is highest in the centre of the imaginal wing disc, showing that this region is subjected to the highest compression. Figure taken from [6].

MOX Technical Reports, last issues

Dipartimento di Matematica
Politecnico di Milano, Via Bonardi 9 - 20133 Milano (Italy)

- 01/2016** Domanin, M.; Buora, A.; Scardulla, F.; Guerciotti, B.; Forzenigo, L.; Biondetti, P.; Vergara, C.
Computational fluid-dynamic analysis of carotid bifurcations after endarterectomy: closure with patch graft versus direct suture
- 02/2016** Crivellaro, A.; Perotto, S.; Zonca, S.
Reconstruction of 3D scattered data via radial basis functions by efficient and robust techniques
- 03/2016** Tarabelloni, N.; Ieva, F.
On Data Robustification in Functional Data Analysis
- 62/2015** Signorini, M.; Zlotnik, S.; Díez, P.
Proper Generalized Decomposition solution of the parameterized Helmholtz problem: application to inverse geophysical problems.
- 63/2015** Lancellotti, R.M.; Vergara, C.; Valdetaro, L.; Bose, S.; Quarteroni, A.
Large Eddy Simulations for blood fluid-dynamics in real stenotic carotids
- 61/2015** Tagliabue, A.; Dedè, L.; Quarteroni, A.
Fluid dynamics of an idealized left ventricle: the extended Nitsche's method for the treatment of heart valves as mixed time varying boundary conditions
- 60/2015** Perotto, S.; Reali, A.; Rusconi, P.; Veneziani, A.
HIGAMod: A Hierarchical IsoGeometric Approach for MODel reduction in curved pipes
- 59/2015** Menafoglio, A.; Guadagnini, A.; Secchi, P.
Stochastic Simulation of Soil Particle-Size Curves in Heterogeneous Aquifer Systems through a Bayes space approach
- 58/2015** Iapichino, L.; Rozza, G.; Quarteroni, A.
Reduced basis method and domain decomposition for elliptic problems in networks and complex parametrized geometries
- 57/2015** Wilhelm, M.; Dedè, L.; Sangalli, L.M.; Wilhelm, P.
IGS: an IsoGeometric approach for Smoothing on surfaces